

EECE 5554 Robotics Sensing and Navigation

Lab 3: IMU

Carlos Anzola

Abstract

This report examines the noise characteristics of a VN-100 IMU/AHRS under stationary conditions using data collected at a 40 Hz rate for 20 minutes and 5 hours. Time series, histograms, power spectral density, and Allan variance plots were used to assess sensor noise. The noise densities for the accelerometer, gyroscope, and magnetometer showed discrepancies from the manufacturer's specifications, with differences potentially attributed to factors such as sampling rate, calibration, environmental conditions, interference, and testing procedures.

Methods

IMU Driver. Data was collected using a custom ROS-based driver for the VN-100 IMU/AHRS. The driver reads data streams via a serial connection from the IMU and is designed to parse only VNYMR data, which includes relevant sensor outputs. After parsing, the driver publishes the following data fields to a ROS topic: 3-axis orientation (in degrees), linear acceleration (in m/s²), angular velocity (in rad/s), and magnetic flux density (in Tesla), along with a timestamped header.

Data Collection. Two datasets were recorded under stationary conditions. The first dataset was collected over 25 minutes, and the second over a 5-hour period. During both sessions, the IMU was kept stationary and as isolated from external sources of interference as possible, including nearby electronic devices, vibrations, and moving objects, to minimize environmental noise.

Data Processing. Outliers were handled in both datasets by using z-scores, as the histograms indicated a normal distribution. Specifically, outliers were defined as points with z-scores exceeding ± 3 standard deviations. These outliers were replaced with the median value of the respective dataset entry to reduce the influence of extreme values on

subsequent analyses, as the median is less sensitive to outliers compared to the mean [1].

Additionally, the respective unit conversions were applied to keep consistency with the required units prior to publishing the ROS message and during the noise characterization analysis.

Noise Characterization. Initially, the time series of each entry of the dataset was plotted to visualize sensor behavior over time. Histograms were then obtained to evaluate the distribution of the samples, and to confirm the normality assumption.

Next, the power spectral density (PSD) was calculated using the Fast Fourier Transform (FFT) to derive the noise density:

$$PSD(f) = \frac{1}{N} \left| \sum_{n=0}^{N-1} x_n e^{-i2\pi f n \Delta t} \right|^2$$

where x_n is the sample value, N is the number of samples, and f is the frequency.

The noise density was calculated using the following equation [2]

$$ND = \sqrt{\text{mean}(PSD(f))}$$

These equations were applied only to the 25-minute dataset, as the Allan variance method computes noise density for the 5-hour dataset.

Finally, the Allan variance, which quantifies the stability of the sensor over time, is defined as [3]

$$\sigma_\eta^2(\tau) = \frac{1}{2N} \sum_{i=0}^N z_i(\tau)$$

Where $z_i(\tau)$ is a 2 sample Bessel-corrected variance given by

$$z_i(\tau) = y_i^2(\tau) + y_{i-1}^2(\tau) - \frac{1}{2} (y_i(\tau) + y_{i-1}(\tau))^2$$

Here, $y_i(\tau)$ represents the slope between samples taken τ seconds apart.

Results

Figures 1 through 4 show the time series for the orientation, accelerometer, gyroscope, and magnetometer data. Overall, the outputs from all the sensors are very stable, and have fluctuations within narrow ranges.

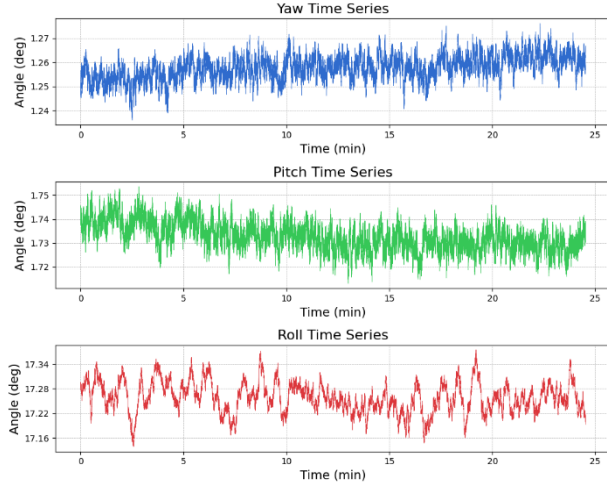


Figure 1. Orientation time series.

Yaw shows a subtle upward drift, while pitch exhibits a gradual downward trend. However, given the relatively short duration of this dataset (25 minutes), these trends have minimal impact on the results, as the overall fluctuation range remains within approximately 0.03° for both yaw and pitch.

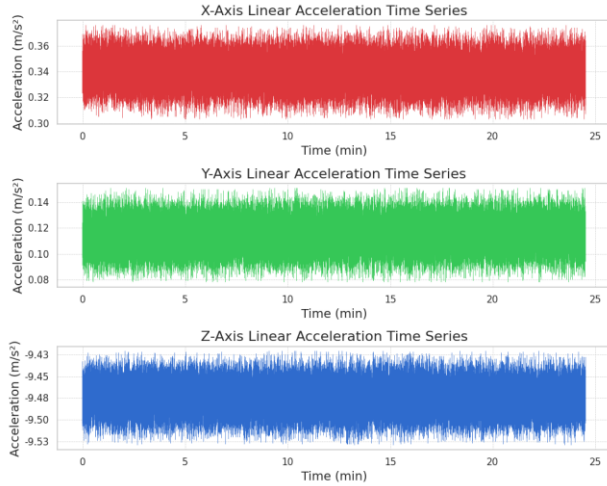


Figure 2. Accelerometer time series.

The accelerometer time series plots confirm that the accelerometer is functioning as expected, capturing the static linear acceleration while showing the influence of Earth's gravitational pull on the Z-axis.

The data is consistent with the behavior of a stationary IMU, where no significant acceleration is present beyond the inherent noise.

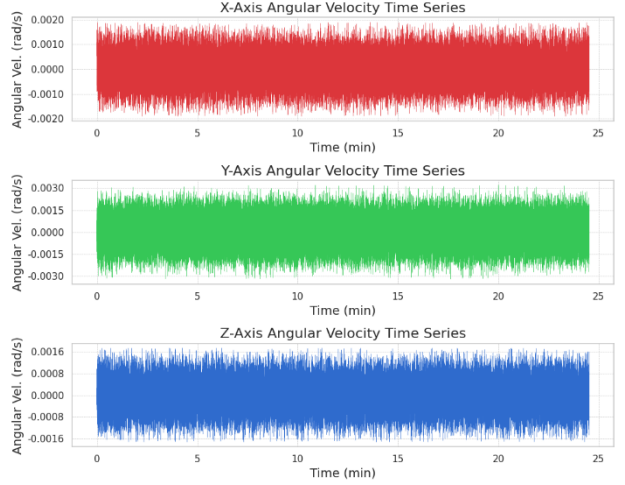


Figure 3. Gyroscope time series.

Similarly, the gyroscope time series plots show consistent values around 0 rad/s across all axes. The fluctuations remain within narrow ranges, indicating minimal noise and confirming that no significant rotational movement occurred during data collection. This behavior aligns with the expected performance of the sensor when at rest.

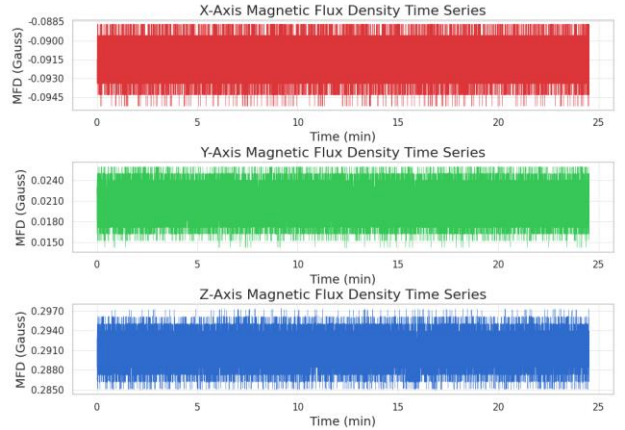


Figure 4. Magnetometer time series.

The magnetometer time series also looks very consistent over time, but the variations seem more limited to specific values. This effect is better illustrated in Figure 8.

Figures 5 through 8 illustrate the histograms for the data across all axes. While the distributions appear to follow a normal pattern in every plot except for the magnetometer, the latter reveals distinct periodic

peaks. These anomalies may be attributed to magnetic interference from the environment, possibly due to nearby, unidentified magnetic sources present during testing, or they could indicate a limitation in the sensor's resolution.

Although the onboard hard/soft iron estimator is designed to automatically compensate for magnetic distortions without requiring user intervention [4], this feature can be disabled if manual calibration is required. It is unknown whether this feature had been disabled before testing. Additionally, as per the lab instructions, no calibration was performed prior to data collection.

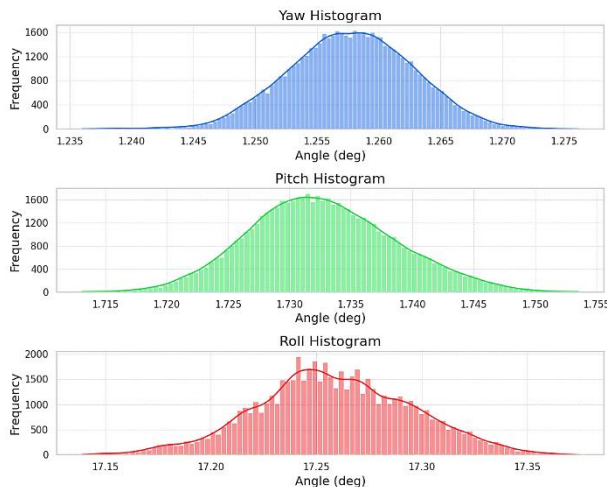


Figure 5. Orientation histograms.

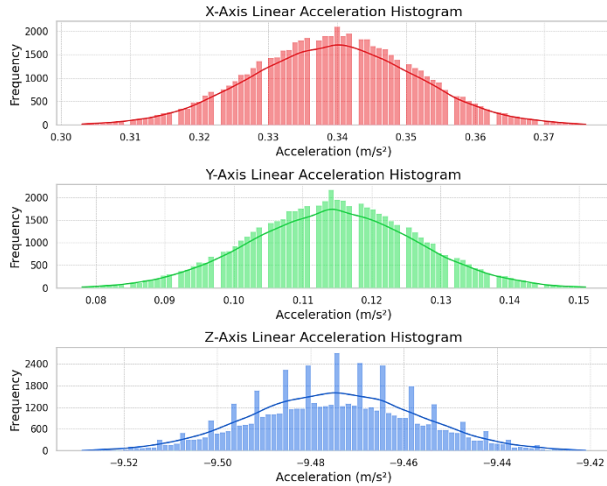


Figure 6. Accelerometer histograms.

The linear acceleration histograms shown in Figure 6 display a generally normal distribution; however, some bars are noticeably underrepresented, while others are disproportionately large. This, combined with the observations from the magnetometer analysis, suggests that sensor resolution may significantly influence these trends, indicating the sensor's inability to register values within certain ranges.

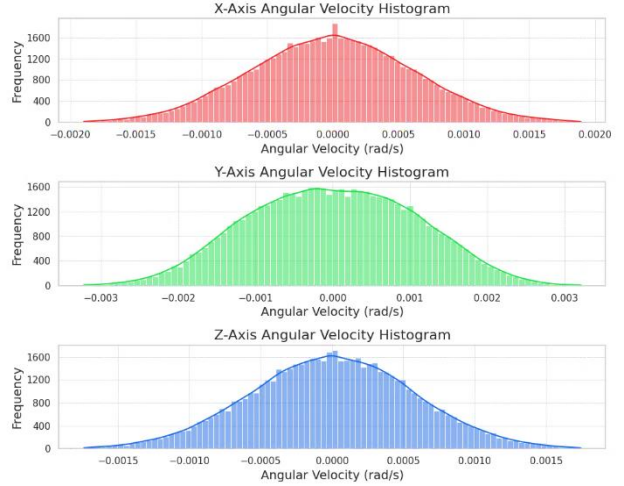


Figure 7. Gyroscope histograms.

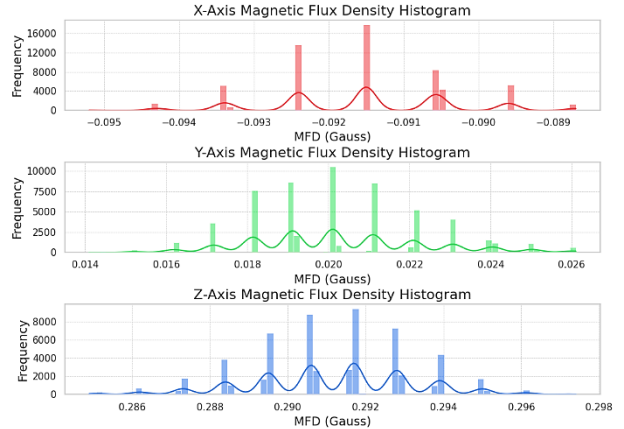


Figure 8. Magnetometer histograms.

A summary of the statistics (mean and standard deviation) for the 25-minute dataset is presented in Table 1. Overall, the mean values are consistent with expected sensor readings, indicating that the IMU performed reliably during the test. The standard deviations are relatively low, suggesting minimal variability in the measurements across the data collection period.

Sensor	Axis	Mean	Standard Dev.
Orient (°)	X	1.2871	0.0052
	Y	1.7731	0.0061
	Z	17.6549	0.0394
Accel (m/s ²)	X	0.3395	0.0121
	Y	0.1144	0.0121
	Z	-9.4747	0.0178
Gyro (rad/s)	X	-0.000004	0.000621
	Y	0.000001	0.001073
	Z	0.000002	0.000574
Mag (μGauss)	X	-0.091538	0.001217
	Y	0.020286	0.002127
	Z	0.291164	0.002087

Table 1. Time series statistics.

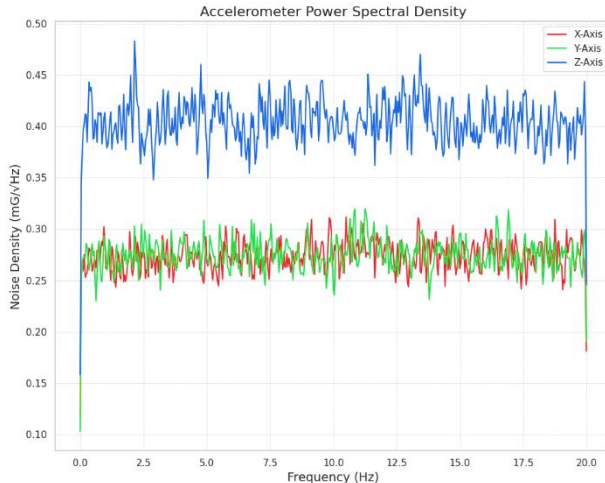


Figure 9. Accelerometer Power Spectral Density.

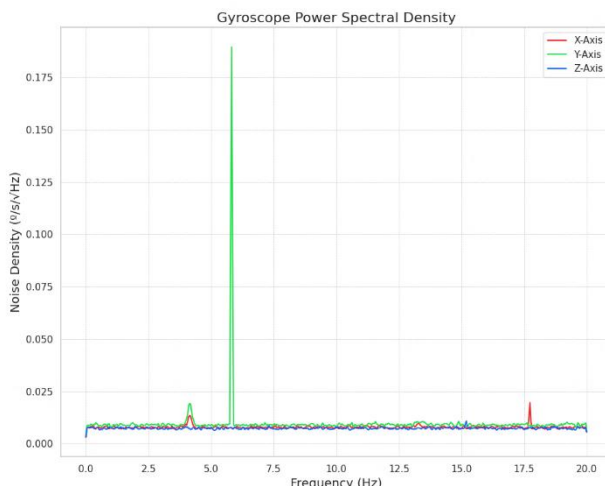


Figure 10. Gyroscope Power Spectral Density.

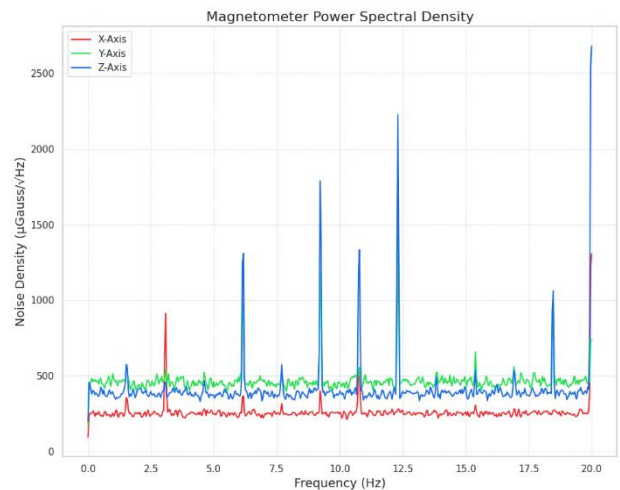


Figure 11. Magnetometer Power Spectral Density.

As an extra step to assess the data in the 25-minute period, the power spectral density (PSD) shown in Figures 9 through 11 was calculated. These values were then utilized to derive the noise density for each axis, which was subsequently averaged for comparison with the specifications provided in the device documentation [5].

Table 2 shows the summary of the calculated noise density values, and the reported values on the VM-100 specifications.

Sensor	Noise Density (Calculated)	Noise Density (Reported)	Units
Accel	0.31	0.14	mg/sqrt(Hz)
Gyro	0.0083	0.0035	°/s/sqrt(Hz)
Mag	382	140	μGauss/sqrt(Hz)

Table 2. Noise density statistics.

The calculated noise densities are roughly twice as high as those specified in the documentation. This variation could come from differences in the testing environments, hardware configurations, and software setups, all of which remain unspecified in the documentation. Further research is required to determine the actual cause of such discrepancies between the results and reported specifications.

Figures 12 through 14 show the Allan Deviation and noise parameter plots for the accelerometer.

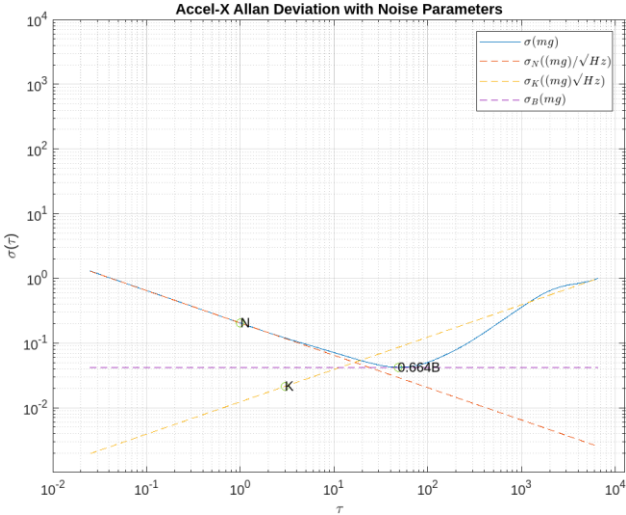


Figure 12. Accelerometer X-axis AVAR plot.

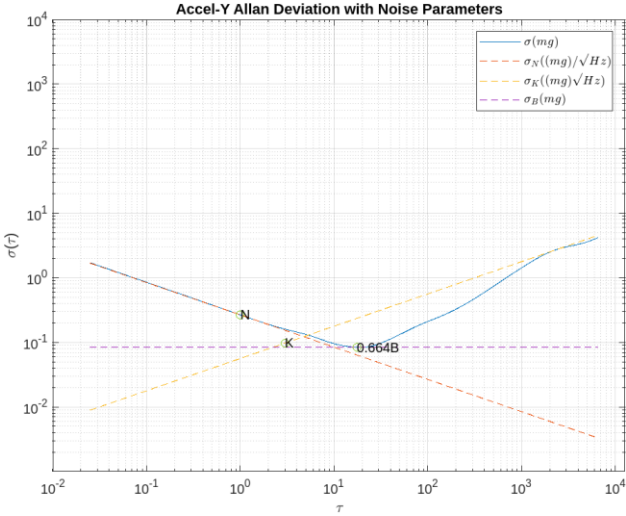


Figure 13. Accelerometer Y-axis AVAR plot.

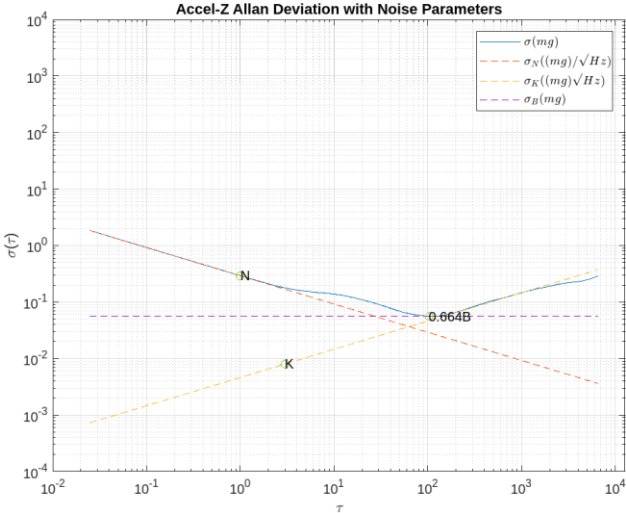


Figure 14. Accelerometer Z-axis AVAR plot.

A summary of the results and comparison with the reported values on the documentation is shown in Table 3.

Accelerometer AVAR Results					
Calculated (Average)			Reported		
N (mg/\sqrt{Hz})	K (mg\sqrt{Hz})	B (mg)	N (mg/\sqrt{Hz})	B (mg)	
0.25	0.04	0.09	0.14	< 0.04	

Table 3. Accelerometer AVAR results.

From the Allan deviation plots, the negative slope of the linear region indicates the presence of Gaussian white noise in every axis. The noise density value (N) calculated is also approximately double than reported. This higher noise density further reinforces the idea that environmental factors or the testing setup might have influenced the performance of the accelerometer.

On the other hand, the positive slope of the linear region, indicates the presence of flicker noise. While the documentation does not provide a value for flicker noise, it is important to note that the absence of this information limits the complete characterization of the noise profile in long-term applications.

In terms of bias stability, the calculated bias stability value (B) is higher than the reported value in the specifications (measured at the point where the Allan deviation plot flattens out after the initial region of Gaussian white noise). Bias stability “is a measure of how the bias will drift during operation over time at a constant temperature” [6]. The difference between results suggests that the accelerometer may exhibit greater drift or noise under the testing temperature employed in this study compared to the official test temperature, which is not specified in the documentation.

Figures 15 through 17 display the Allan deviation and noise parameter plots for the accelerometer. A summary of the results, alongside a comparison with the reported values from the documentation, is presented in Table 4.

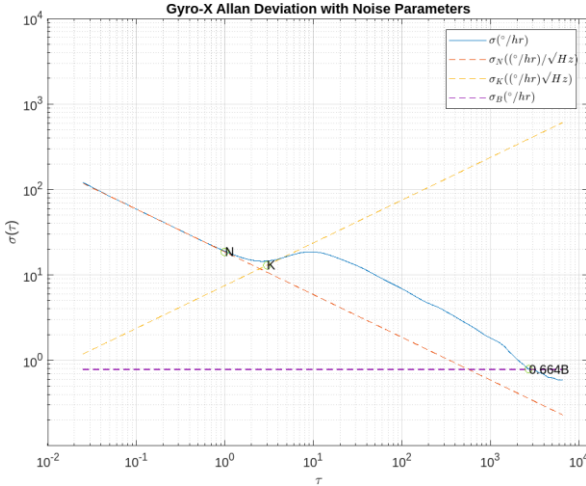


Figure 15. Gyroscope X-axis AVAR plot.

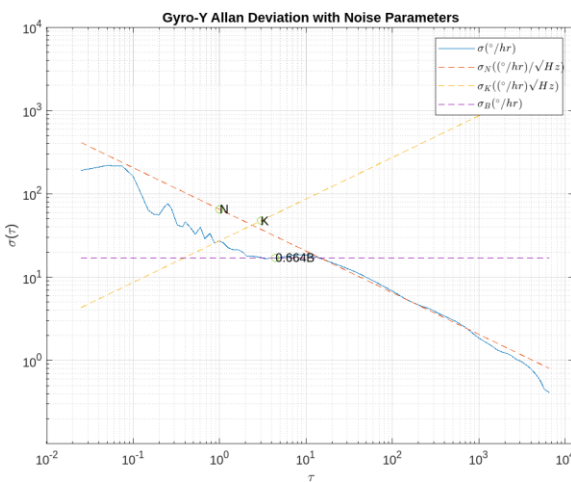


Figure 16. Gyroscope Y-axis AVAR plot.

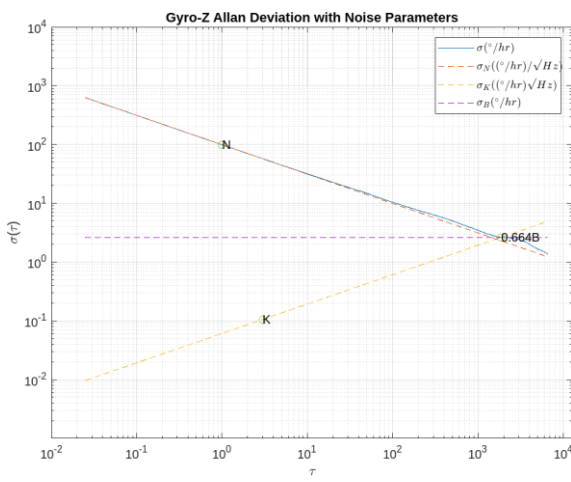


Figure 17. Gyroscope Z-axis AVAR plot.

Gyroscope AVAR Results					
Calculated (Average)			Reported		
N (°/hr/√Hz)	K (°/hr/√Hz)	B (°/hr)	N (°/hr/√Hz)	B (°/hr)	
0.0170	20.16	10	0.0035	< 10	

Table 4. Gyroscope AVAR results.

The gyroscope Allan deviation plots show notable differences compared to the accelerometer results. In particular, the Y-axis plot reveals an oscillatory pattern, indicating the presence of quasi-sinusoidal noise [7]. This type of noise occurs when periodic or near-periodic components are added to the sensor's random noise profile, possibly due to environmental factors such as vibrations or electrical interference.

Similar to the accelerometer, the gyroscope exhibits Gaussian white noise, as indicated by the initial negative slope in the Allan deviation plots. However, the calculated noise density for the gyroscope exceeds the values reported in the manufacturer's specifications, suggesting that external factors or testing conditions may have contributed to higher noise levels.

The bias stability closely aligns with the reported value, although the calculated result is slightly above the typical specification of <5°/hr. This indicates that while the gyroscope performs well in terms of stability, some degree of drift is present under the testing conditions.

By deriving key parameters such as noise density and bias stability from the Allan variance analysis, the VM-100 can be accurately modeled for simulation purposes. These parameters help represent the IMU's real-world performance, allowing for more realistic simulations in various applications.

Despite some discrepancies with the reported specifications, the overall results reflect a robust performance by the IMU. The relatively low levels of noise and drift, combined with consistent data across different axes, suggest that the embedded filtering and signal processing algorithms are functioning effectively, contributing to the IMU's reliable operation.

References

- [1] Pennsylvania Department of Education, "PA Department of Education," June 2011. [Online]. Available: <https://www.education.pa.gov/K-12/Career%20and%20Technical%20Education/Documents/Electrical%20T-Chart%20-%20Describe%20how%20outliers%20affect%20measures%20of%20central%20tendency.pdf>.
- [2] M. Wrona, "Michael Wrona's Blog," 15 May 2021. [Online]. Available: <https://mwrona.com/posts imu-psd/>.
- [3] D. Morris, "Tangram Vision," 19 December 2023. [Online]. Available: <https://www.tangramvision.com/blog/the-allan-deviation-and-imu-error-modeling-part-4-of-5>.
- [4] VectorNav, "VECTORMNAV," 2017. [Online].
- [5] VectorNav, "VECTORMNAV," [Online]. Available: <https://www.vectornav.com/products/detail/vn-100>.
- [6] VectorNav, "VECTORMNAV," [Online]. Available: <https://www.vectornav.com/resources/inertial-navigation-primer/specifications--and--error-budgets/specs-imuspecs>.
- [7] D. A. Howe, "Interpreting oscillatory frequency stability plots," in *Proceedings of the 2002 IEEE International Frequency Control Symposium and PD*, 2002.